Opto-Electronic Advances

ISSN 2096-4579 CN 51-1781/TN

Complete-basis-reprogrammable coding metasurface for generating dynamically-controlled holograms under arbitrary polarization states

Zuntian Chu, Xinqi Cai, Ruichao Zhu, Tonghao Liu, Huiting Sun, Tiefu Li, Yuxiang Jia, Yajuan Han, Shaobo Qu and Jiafu Wang

Citation: Chu ZT, Cai XQ, Zhu RC, et al. Complete-basis-reprogrammable coding metasurface for generating dynamically-controlled holograms under arbitrary polarization states. *Opto-Electron Adv* **7**, 240045(2024).

https://doi.org/10.29026/oea.2024.240045

Received: 27 February 2024; Accepted: 12 June 2024; Published online: 26 July 2024

Opto-Electronic Advances

Article

September 2024, Vol. 7, No. 9

DOI: 10.29026/oea.2024.240045

Complete-basis-reprogrammable coding metasurface for generating dynamically-controlled holograms under arbitrary polarization states

Zuntian Chu[1,2†], Xinqi Cai[1,2†], Ruichao Zhu[1,2*], Tonghao Liu[3*], Huiting Sun[1,2], Tiefu Li[1,2], Yuxiang Jia[1,2], Yajuan Han[1,2], Shaobo Qu[1,2] and Jiafu Wang[1,2*]

Reprogrammable metasurfaces, which establish a fascinating bridge between physical and information domains, can dynamically control electromagnetic (EM) waves in real time and thus have attracted great attentions from researchers around the world. To control EM waves with an arbitrary polarization state, it is desirable that a complete set of basis states be controlled independently since incident EM waves with an arbitrary polarization state can be decomposed as a linear sum of these basis states. In this work, we present the concept of complete-basis-reprogrammable coding metasurface (CBR-CM) in reflective manners, which can achieve independently dynamic controls over the reflection phases while maintaining the same amplitude for left-handed circularly polarized (LCP) waves and right-handed circularly polarized (RCP) waves. Since LCP and RCP waves together constitute a complete basis set of planar EM waves, dynamically-controlled holograms can be generated under arbitrarily polarized wave incidence. The dynamically reconfigurable meta-particle is implemented to demonstrate the CBR-CM's robust capability of controlling the longitudinal and transverse positions of holograms under LCP and RCP waves independently. It's expected that the proposed CBR-CM opens up ways of realizing more sophisticated and advanced devices with multiple independent information channels, which may provide technical assistance for digital EM environment reproduction.

Keywords: basis vector control; reprogrammable metasurface; dynamically-controlled holograms; arbitrary polarization state; broadband

Chu ZT, Cai XQ, Zhu RC et al. Complete-basis-reprogrammable coding metasurface for generating dynamically-controlled holograms under arbitrary polarization states. *Opto-Electron Adv* **7**, 240045 (2024).

Introduction

Decades of advanced and diverse progresses in metasurfaces, the judiciously engineered planar arrays composed of periodically or quasi-periodically arranged sub-wavelength resonant building blocks (meta-particles), hold giant promise for elaborate wave-object

[1]Shaanxi Key Laboratory of Artificially-Structured Functional Materials and Devices, Air Force Engineering University, Xi'an 710051, China; [2]Suzhou Laboratory, Suzhou 215000, China; [3]Zhijian Laboratory, Rocket Force University of Engineering, Xi'an 710025, China.

[†]These authors contributed equally to this work.

*Correspondence: RC Zhu, E-mail: zhuruichao1996@163.com; TH Liu, E-mail: liutonghaor@163.com; JF Wang, E-mail: wangjiafu1981@126.com

Received: 27 February 2024; Accepted: 12 June 2024; Published online: 26 July 2024

interaction[1–5]. As an emerging platform, given the merits of simple and compact fabrication and powerful on-demand capabilities, metasurfaces have transcended the limitations of conventional materials, provided innovative and extraordinary flexible control methodologies for amplitude[6,7], phase[8], polarization[9,10], and transmission mode[11] of electromagnetic (EM) waves across the whole spectrum, and explored various fascinating applications including hybrid-dispersion metalens[12,13], holographic imaging display[14], information encryption and storage[15], and wireless communications[16,17]. With the further development of modern multi-target integrated equipment and multi-task processing systems, many efforts are being devoted to the exploitation and expansion of multiplexed metasurfaces capable of merging multiple EM functionalities into a single shared-aperture configuration, where the degrees of freedom (DOFs) utilized for manipulating EM waves include polarization, wavelength, incident angle, transmission direction and orbital angular momentum (OAM). Decorrelated and controllable EM modulation channels can be integrated into single metasurface platform, e.g., polarization-insensitive anisotropic meta-particles for achieving independent orthogonal linearly polarized (LP) wavefronts customization[18], differential transmission of orthogonal circularly polarized (CP) wavefronts assisted by two-dimensional (2D) or three-dimensional (3D) chiral structures or multiple phase modulations[19,20], full-space asymmetric transmission (AT) enabled via multi-layered composite Janus metasurface[21,22], off-axis cylindrical vector beam (CVB) generation[23], vector visual cryptography (VC)[24], and elliptical polarization beam splitters[25]based on compound phase modulation. Though plenty of versatile metasurfaces have entered human's vision so far, most of them are passive and static, leading to fixed functionalities and characteristics once fabricated while limiting the adaptability to external time-varying environment. Aiming at offering dynamic propagation manipulation and real-time information delivery for EM waves, the appearance and excavation of active and tunable metasurfaces effectively surmounts the above conundrum and implements eye-catching achievements.

Initially, the concept of digital and reprogrammable coding metasurfaces (RCMs) has been put forward by Cui et al., which establishes sound foundation for controlling EM waves propagation in real time[26]. Compared with the metasurfaces with continuously various parameters, the digital coding metasurfaces (DCM) adopt binary codes to quantify physical parameters (e.g., amplitude, phase, and polarization), making them possible to design the EM waves simply and conduct complicated EM operations. In light of digital signal processing, the scattering pattern shift of DCM has been deduced via utilizing convolution theorem in Fourier transform to guide arbitrary beam directions in upper 3D half space with little distortion[27]. Moreover, both concepts of information entropy and addition theorem are introduced into DCM respectively, which not only provides guidance for the control of coding mode and scattering mode, but also reveals the internal relationship of different bit codes[28,29]. In terms of multi-physical manipulation, these fascinating concepts are also successfully transitioning from microwave to sound fields, mechanical fields, and temperature fields based on altering different material regimes or changing unit architecture models[30–32]. An inspirational work that combines functional dynamic phase with specified rotation angles provides a simplified framework to assemble a polarization-reversible metalens in terahertz region, promoting the transformation from DCM to RCM[33]. It's noteworthy that in microwave region, the qualitative leap from DCM to RCM can be achieved with the loading of active components controlled by electric bias, optical switch, mechanical actuation, and the like while the coding sequences are dynamically regulated by the field-programmable gate array (FPGA), which extremely enhances the DOFs of metasurfaces and promotes the synthetical and intelligent applications of EM waves manipulation[34–37]. Through cyclic switching a group of coding sequences in a pre-designed period, the desired harmonic beam power distributions are yielded and the joint modulation of RCM in temporal and spatial domains is achieved[38]. A series of polarization-modulated information metasurfaces and multi-channel RCMs in transmission/reflection mode are constructed with the assistance of amplitude-phase-joint-coding technique and orthogonal-polarization-coding technique[39–42]. Furthermore, intelligent applications such as adaptive perception, autonomous decision making and programmable diffraction deep neural network are realized via introducing sensing modules and intelligent algorithms into RCMs[43,44]. However, most existing RCMs are only suitable for incident waves in LP basis form or hard to identify the incident polarization to dynamically carry out functionalities. Meanwhile, the reconfigurable meta-particles tuned in one-dimensional (1D) construction significantly reduce the DOF and are unable to be

employed to complex wavefront generation, and the currently individually addressable techniques in 2D configuration generically require multiple active components and multi-layered cascaded metasurfaces, which sacrifices part of the available space and cannot meet the needs of miniaturized and integrated systems.

Among multitudinous studies of wavefronts shaping via RCMs, the most remarkable application is undoubtedly reprogrammable meta-holograms (RMHs), on-demand recording, storage, and evocation of the target images, which holds great potential ranging from information encryption to intelligent detection[45]. RHMs are essentially dynamic meta-holograms according to the classification of holograms. As known, static meta-holograms mean that only one fixed image can be reconstructed by meta-elements, while dynamic meta-holograms mean that multiple different holographic images can be reconstructed due to the variations in the incident light, or the meta-particle configuration, or relative distances between two adjacent metasurfaces. For instance, on the one hand, many fundamental properties of the light act as independent dimensions, such as the amplitude, phase, polarization, wavelength, and propagation direction, which enables multiplexing technologies to integrate different holographic images[46–51]. On the other hand, an external input stimuli applied to metasurfaces consisting of active materials is utilized to switch reconstructed holographic images[52,53]. Also, the distinguished methods including inverse design based on machine learning can assist researchers in designing meta-holograms that possess desired optical responses and multiple DOFs[54]. A series of creative achievements in the field of micro and nano have also driven the study of RMHs in the microwave band. Specifically, the first groundbreaking RMH with high-resolution and low-noise characteristics is demonstrated via reflecting the amplitude and phase distributions optimized by improved Gerchberg–Saxton (GS) algorithm[55]. Subsequently, the organic combination of machine learning and 2-bit RCM can directly capture high-quality imaging and high-precision target detection[56]. When electronically controlled PIN diodes are loaded with different bias voltages, two-polarization-channel tunable dynamic RMHs are vividly exhibited in transmission and reflection mode, respectviely[57]. Thanks to chiral effect, the embedded rheostatic diodes in mirror positions of the split-ring metallic resonator, flexibly switch spin-multiplexing meta-holograms and low observable refection[58]. Nevertheless, either the RMHs under excitation of CP waves are neglected or most are operated in one dimension, or the coupling between manipulating orthogonal CP basis is inevitable, which undoubtedly reduces the simplicity of meta-particles construction and increases the difficulty of metasurface treatment. Hence, the research of this academic issue still needs to be further explored.

In this work, we propose an innovative methodology of complete-basis-reprogrammable coding metasurface (CBR-CM), which enables on-demand independent and dynamic holographic patterns reconstruction under arbitrary polarization states leveraging dynamically reconfigurable meta-particle. Through individually introducing two symmetrical positive–intrinsic–negative (PIN) diodes into the umbrella-shaped structure whose equivalent circuit can be altered via switching the supply voltages controlled by FPGA, the dynamic Aharonov-Anandan (AA) phase induced via path effect is motivated to encode the 1-bit co-polarized reflection phase responses maintaining the same amplitudes of LCP and RCP waves when separately switching the “ON/OFF” states of the left and right PIN diodes. Furthermore, according to the coding sequences calculated through improved holographic optimization algorithm, the EM waves under orthogonal CP basis can be excited and modulated respectively, ingeniously avoiding the unnecessary coupling and crosstalk between dual CP co-polarized reflection channels. As proof-to-concept, a broadband (9–10.5 GHz) and ultracompact ($0.148\lambda_0$ at 10 GHz) CBR-CM prototype is designed and fabricated, and four illustrative functions are demonstrated in both simulations and experiments, including spin-controlled meta-holograms with identical or variable focal length, coplanar dual-polarized pixel synthesis, and full-polarized detection system on Poincaré sphere with the assistance of vectorial decomposition and synthesis, which generically and respectively prove the independent spin-space-addressing-multiplexing capability and puissant arbitrary polarization state adaptability in dynamic holograms. Encouragingly, the proposed complete-basis-reprogrammable coding paradigm could be easily extended to other spectra and open a promising window for full-featured RCMs-based meta-holograms.

Results and discussion

Figure 1 exhibits the schematic diagram of the proposed CBR-CM to achieve spin-integrated manipulation of EM waves at upside of the interface. For independent and

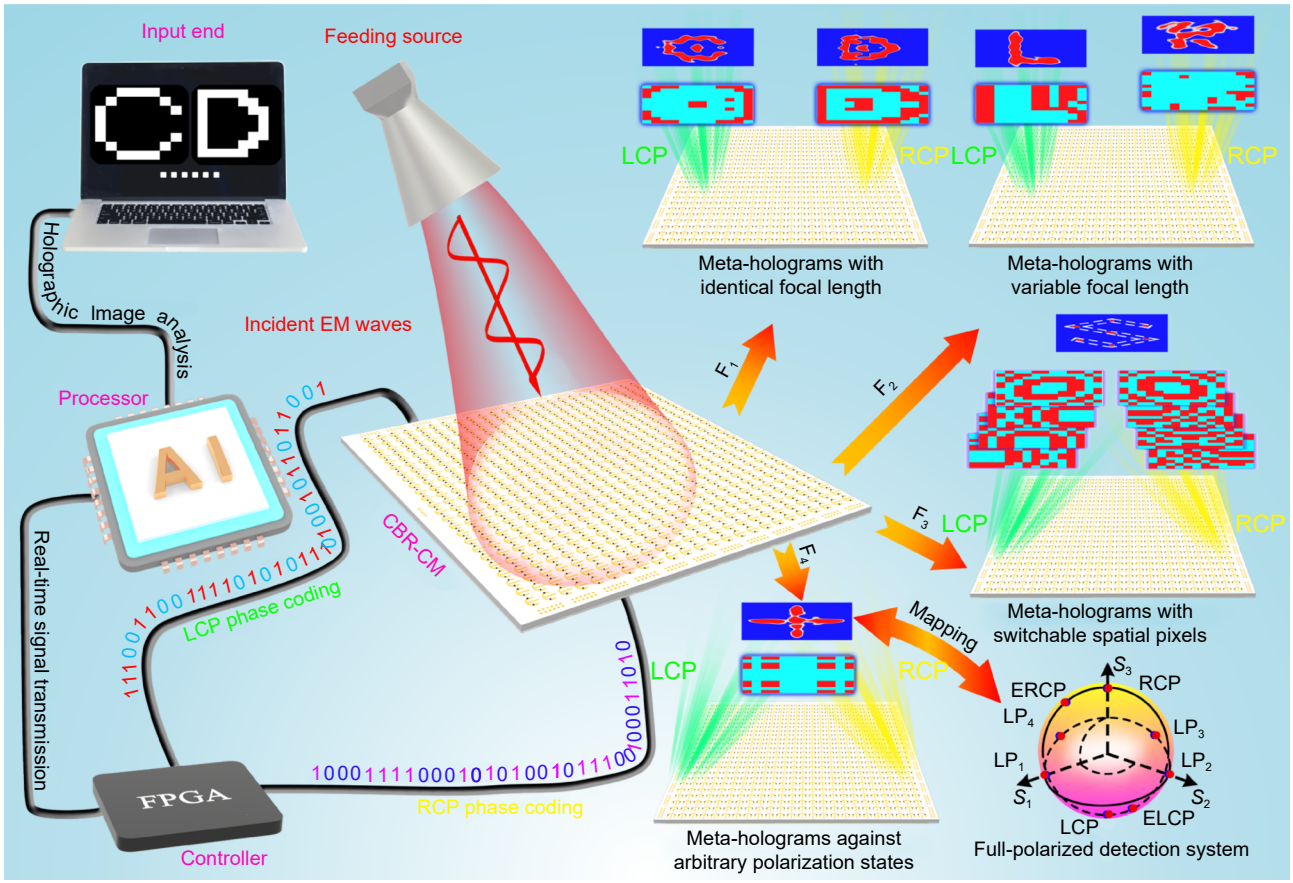

Fig. 1 | Schematic illumination of the CBR-CM. The CBR-CM is constructed via symmetrically incorporating PIN diodes into an elaborately designed metasurface structure, and these diodes are controlled by multi-channel bias voltages provided by a FPGA-based control circuit connected to real-time holographic processing system. As illustrated examples, by arranging specific LCP and RCP 1-bit coding sequences, dynamic meta-holograms with identical focal length, variable focal length, switchable spatial pixels, and against arbitrary polarization state are successively demonstrated.

real-time control of orthogonal CP co-polarized reflected wavefronts at microwave frequencies, each meta-particle of CBR-CM, consisting of umbrella-shaped structure incorporated with PIN diodes, is designed to modulate the reflection phase responses under orthogonal CP incidence. When the PIN diode embedded into the left arm works on the "ON" (or "OFF") state, the co-polarized reflection phase responses of the meta-particles are encoded as "1" (or "0") under LCP incident waves. Similarly, with or without PIN diodes embedded into the right arm activated, the co-polarized reflection phase responses are encoded as "1" (or "0") under RCP incident waves, respectively. A control circuit based on FPGA receiving instructions from holographic processing system and sending data stream is then fabricated and introduced to multiple bias voltage channels for CBR-CM, making each meta-particle individually addressable to dynamically operate as a sub-reflector with broadband and dynamic phase modulation capability. Accordingly, the CBR-CM possesses 2D spatial DOF of modulating dual-channel reflection phase coding patterns. By further employing improved holographic optimization algorithm to design LCP and RCP 1-bit reflection coding sequences, four illustrative functions are demonstrated dynamically based on a single CBR-CM prototype. In the first three demonstrations, spin-controlled meta-holograms with identical and variable focal length, coplanar dual-polarized pixel synthesis are realized via tuning different coding sequences of orthogonal CP channels. In the last demonstration, full-polarized detection system is constructed through encoding the same sequences and extracting amplitude-phase information of orthogonal CP channels.

Meta-particle design and underlying mechanism

As a practical implementation in the microwave frequency

band, here, a dynamically reconfigurable meta-particle whose co-polarized reflection phases of the LCP and RCP incident waves can be simultaneously and independently controlled is punctiliously designed, as illustrated in Fig. 2(a). The meta-particle is arrayed in a square periodic lattice spaced at P=10 mm, and comprises four metal layers (copper, thickness t=0.035 mm), two substrates, and a bonding film. The side view of the meta-particle is portrayed in Fig. 2(b). The patch layer (umbrella-shaped structure, radius r=3.8 mm) and the metal backplate as middle ground of the meta-particle are etched on two sides of the top substrate (F4B, loss tangent tanσ=0.001, dielectric constant ε_r=2.65, thickness h_1=4 mm). The direct current (DC) bias networks for controlling co-polarized reflected waves under RCP and LCP incidence are etched on two sides of the bottom substrate (F4B, loss tangent tanσ=0.001, dielectric constant ε_r=2.65, thickness h_3=0.25 mm). Two substrates are eventually bonded together with a bonding film (Rogers RO4450F, loss tangent tanσ=0.003, dielectric constant ε_r=3.52, thickness h_2=0.18 mm). The widths of the umbrella-shaped structure and the bias line connecting to it are w_1=0.8 mm and w_2=0.7 mm, and the other parameters shown in the meta-particle are α=70°, β=130°, d_1=0.6 mm, d_2=0.9 mm. Two PIN diodes (Skyworks, SMP1320-040LF) are embedded mirror-symmetrically on the left- and right-arm of the umbrella-shaped structure, and the equivalent circuits are exhibited in Fig. 2(c), in which the values

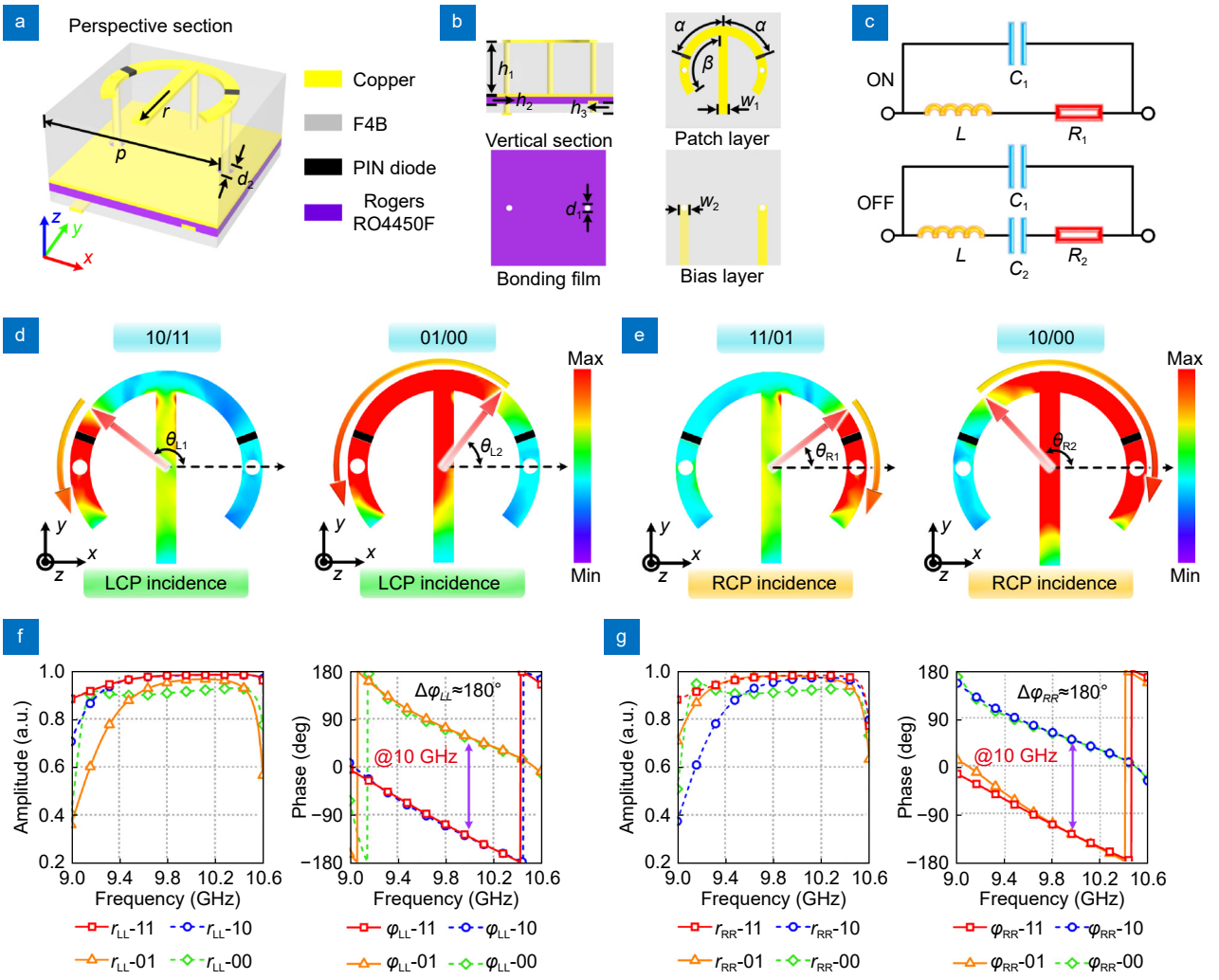

Fig. 2 | Geometric configuration and EM responses of the dynamically reconfigurable meta-particle. (**a**) Perspective view of the proposed meta-particle. (**b**) Vertical and layered schematic of the proposed meta-particle. (**c**) The equivalent circuit models of the PIN diodes in the "ON" and "OFF" states. (**d**) Simulated surface current distributions on the proposed meta-particle of state "11/10" and "01/00" under LCP incidence at 10 GHz. (**e**) Simulated surface current distributions on the proposed meta-particle of state "11/01" and "10/00" under RCP incidence at 10 GHz. (**f**, **g**) Simulated co-polarized reflection amplitude and phase responses of the proposed meta-particle with coding states of "11", "10", "01", and "00" under orthogonal CP normal incidence.

of C_1, C_2, L, R_1, and R_2 are 0.04 pF, 0.05 pF, 2.55 nH, 0.51 Ω, and 0.71 Ω, respectively. To feed these PIN diodes, the left- and right-arm and the top position of the umbrella-shaped structure are separately connected to the bias layer via two through holes and one blind hole.

For the purpose of controlling PIN diodes independently, each meta-particle connects two DC strips that supply different DC bias voltages controlled by FPGA, but is simultaneously grounded for the sake of simplified design. By changing the bias voltages difference of two arms, the conduction and cutoff of PIN diodes can be switched independently, accordingly, the working states of the meta-particle also convert. In the proposed paradigm, each coding meta-particle has four states: "ON/ON", "ON/OFF", "OFF/ON", and "OFF/OFF". The states before and after the symbol "/" represent the states of the PIN diodes in left- and right-arm. Here, we define these four states as digital codes "11", "10", "01", and "00", respectively, in which the former and the latter of the two-bit codes represent the co-polarized reflection phases under the illumination of LCP and RCP wave. With the assistance of a commercial software Computer Simulation Technology (CST) Microwave Studio, we explore the spin-selective performances of the dynamically reconfigurable meta-particle in microwave X band, in which the ON (or OFF) states of PIN diodes are represented by utilizing lumped elements shown in Fig. 2(c). See Materials and Methods for more details of the simulation setup. In Fig. 2(d) and 2(e), the simulated surface currents distributions are illustrated under LCP and RCP incident waves at 10 GHz when the PIN diodes are in ON or OFF states. It's observed that when the PIN diode on the left/right arm is switched from ON ("11" and "10")/("11" and "01") to OFF state ("01" and "00")/("10" and "00"), the surface currents vary as the central angle of the corresponding arm of the path evolution changes, and induce a correlated phase shift. Since the phase shift depends only on the variation of central angle determined by the starting and ending position of the arc trajectory, and the phases generated via the incident orthogonal CP waves will return to initial phase after the cyclic evolution of different closed paths, which entirely coincides with AA geometric phase caused by the rotating Doppler shift in the optical Coriolis effect. According to the path evolution, the co-polarized AA reflection phases of the proposed meta-particles under the excitation of orthogonal CP waves which are derived detailedly in Section S1 (Supplementary information) can be expressed as follows

$$\begin{cases} \Delta\Phi_{\mathrm{LL}}^{\mathrm{AA}} = 2\int_{\theta_{\mathrm{sL2}}}^{\theta_{\mathrm{eL2}}} \mathrm{d}\theta_L - 2\int_{\theta_{\mathrm{sL1}}}^{\theta_{\mathrm{eL1}}} \mathrm{d}\theta_{\mathrm{L}} = 2(\theta_{\mathrm{sL1}} - \theta_{\mathrm{sL2}}) \\ \Delta\Phi_{\mathrm{RR}}^{\mathrm{AA}} = 2\int_{-\theta_{\mathrm{sR2}}}^{-\theta_{\mathrm{eR2}}} \mathrm{d}\theta_{\mathrm{R}} - 2\int_{-\theta_{\mathrm{sR1}}}^{-\theta_{\mathrm{eR1}}} \mathrm{d}\theta_R = 2(\theta_{\mathrm{sR2}} - \theta_{\mathrm{sR1}}) \end{cases}, \tag{1}$$

where θ_{sL1} (θ_{sR1}) and θ_{sL2} (θ_{sR2}), and θ_{eL1} (θ_{eR1}) and θ_{eL2} (θ_{eR2}) represent the starting position and ending position of the surface currents distributions path corresponding to excitation of LCP(RCP) waves. Notably, the positions of the PIN diodes to a large extent influence the co-polarized reflection phase shifts, actually, the co-polarized reflection amplitudes are also affected. Thus, the optimal locations of the PIN diodes should be determined and more details are provided in Section S2 (Supplementary information).

Figure 2(f) shows the co-polarized reflection amplitudes and phases under LCP incident waves when the coding states of "11", "10", "01", and "00" of the proposed meta-particle are carried out. Obviously, the co-polarized phases difference when the left PIN diode is in ON state ("11" and "10") and OFF state ("01" and "00") is almost 180°, which is in coincidence with the calculated $\Delta\Phi_{\mathrm{LL}}^{\mathrm{AA}}\approx180°$ ($\theta_{\mathrm{sL1}}=\theta_{\mathrm{L1}}=143°$ and $\theta_{\mathrm{sL1}}=\theta_{\mathrm{L2}}=53°$), and the amplitudes of reflections are on average at 0.9 in the frequency range of 9–10.5 GHz. In addition, it's noted the simulated co-polarized reflection phases remain almost unchanged and the reflection amplitudes are on average at 0.9 between 9 and 10.5 GHz with different states of the right PIN diode, demonstrating the influence of the right PIN diode can be ignored and the reflection amplitudes and phases are solely modulated by switching ON/OFF of the left PIN diode. Meanwhile, the simulated co-polarized reflection amplitude and phase responses with the illumination of RCP wave are depicted in Fig. 2(g). The difference of the co-polarized reflection phases can attain around 180°, which is in good agreement with the calculated $\Delta\Phi_{\mathrm{RR}}^{\mathrm{AA}}\approx180°$ ($\theta_{\mathrm{sR2}}=\theta_{\mathrm{R2}}=133°$ and $\theta_{\mathrm{sR1}}=\theta_{\mathrm{R1}}=43°$) and the amplitude can also be held on average at 0.9. The effect of the state of the right PIN diode on the co-polarized amplitude and phase of LCP incident wave is also negligible. However, it can be noted that a chiral amplitude response to some extent appears in Fig. 2(f) and 2(g), especially at edge frequencies in the designed frequency band, which is mainly caused by the practical coupling interference between the DC bias network and the patch layer. In particular, the deviation of high co-polarized amplitudes for orthogonal CP

incidence is relatively weak so that it can be neglected in the frequency band of interest in terms of the phase-only meta-holograms. Thus, from the simulated profiles in Fig. 2, it's noted that the proposed meta-particle owns good orthogonal polarization isolation at the microwave frequency band and possesses the faculty to modulate the co-polarized reflection phase responses in two orthogonal CP waves independently and simultaneously. This formalism can be extended to other frequency band, and we further demonstrate the feasibility in terahertz spectra within the working frequency band of 0.8–1.1 THz in Section S3 (Supplementary information). Based on the reflection complex Jones matrix transformation relationship between CP incidence and LP incidence, the four states of meta-particles in the form of complex Jones matrices under CP basis possess unique corresponding state of matrix under LP basis, thereupon, the CBR-CM enables implementation of specifically dynamic wavefronts manipulation in LP reflection channel. More details of the deduction process are listed in Section S4 (Supplementary information).

Directional generation of meta-holograms with identical and variable focal length

To validate the powerful ability of the proposed dynamically reconfigurable meta-particle to reconstruct arbitrary holographic patterns of orthogonal CP waves in co-polarized channels, we design, fabricate, and measure a CBR-CM prototype consisting of a 24×24 array of meta-particles with a total size of 250×260 mm^2 to attain the illustrative examples, which is much larger than the wavelength at the operating frequency. The overall schematics of the CBR-CM prototype, including the top patch layer, the middle ground, the DC bias network for controlling co-polarized reflection waves under RCP and LCP incidence are illustrated in Section S5 (Supplementary information). See Materials and Methods for more details of the prototype fabrication. Commonly, however, achieving microwave hologram in good quality is subjected to the coupling between the complicated metallic structures. Accordingly, the amplitude and phase responses of the periodically arranged pixels single meta-particle deteriorate. Here, each 2×2 identical meta-particles makes up a super-cell as a basic pixel unit with the size of 20×20 mm^2 to be compatible with periodical boundary conditions. Moreover, it's noteworthy that the size of the pixel is still in the sub-wavelength scale. Meanwhile, it should be noted that 2×2 identical meta-particles that make up each pixel are connected via elaborately optimized DC bias junction for saving feeding resources and achieving compact design. More details about the structural configuration and simulated EM responses of the super-cell are provided in Section S6 (Supplementary information). Since each super-cell requires two independent voltages, a FPGA-based control circuit is designed to provide 288 independent voltage channels. See Materials and Methods for more details of FPGA-based control circuit. Correspondingly, we perform the phase-only (PO) meta-hologram simulation and experiment to verify the dual-channel spin-multiplexed modulation characteristic where the iterative optimization algorithm, a phase retrieval method, is applied to calculate the ideal phase profiles with uniform amplitude for reconstructing the target images. By introducing a weighting factor to constantly adjust the phase profiles with fixed amplitude in the metasurface plane, the calculated diffraction field gradually approximates the target images in the iteration process. The design process is provided in Section S7 (Supplementary information).

In the first demonstration, we use the proposed metasurface to generate meta-holograms with identical focal length. Two different target holographic images: letters "C" and "D" are prestored in L_r-L_i channel and R_r-R_i channel, respectively, as shown in the left panel of Fig. 3(a) and 3(b). Both reference frequencies of the channels are chosen at 10 GHz and the holographic imaging plane is designed at z=100 mm apart from the metasurface. The desired phase coding patterns for reconstructing the target images are separately calculated via iterative optimization algorithm and presented in the right panel of Fig. 3(a) and 3(b). For verification, the meta-holograms in pre-defined polarization channels are further conducted full-wave simulation and experimental characterization. See Materials and Methods for more details of the simulation setup and experimental setup. The following sections also employ the same method. The numerically simulated and experimentally measured results at the observational plane of z=100 mm for different channels are shown in Fig. 3(c) and 3(d), from which vivid and iconic holographic images are clearly seen being reconstructed spatially in the near field and in good accordance with the target images. It's worth mentioning that for reducing the diffraction effect of reflected waves and obtain sharper image profiles, the aforementioned super-cell strategy is adopted in constructing the meta-holograms.

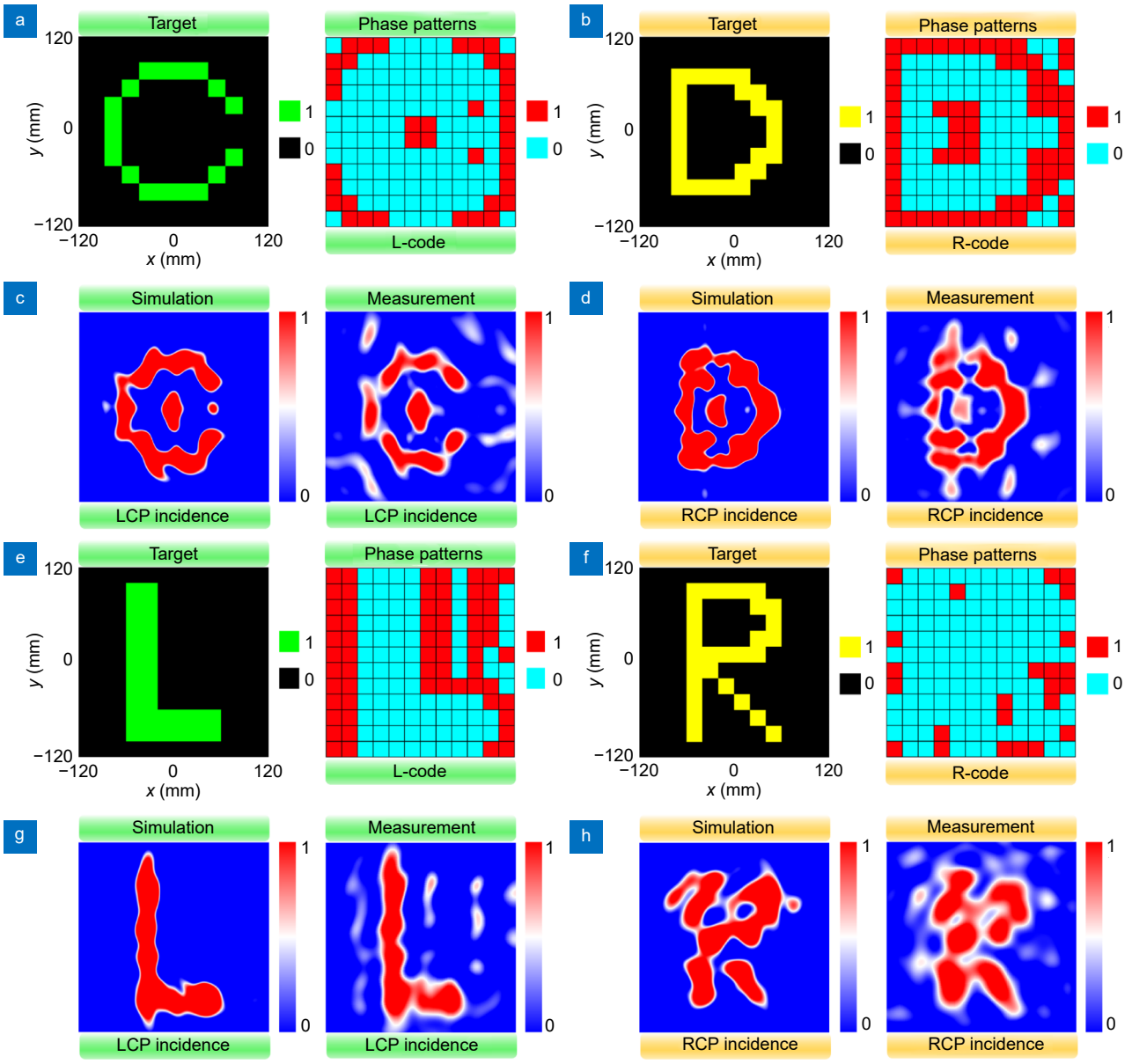

Fig. 3 | Directional generation of meta-holograms with identical and variable focal length. (**a**) The target monochrome image of the letter "C" and corresponding phase coding patterns under the normal incidence of LCP waves. (**b**) The target monochrome image of the letter "D" and corresponding phase coding patterns under the normal incidence of RCP waves. (**c**) Numerically simulated and experimentally measured normalized electric field intensity of LCP component utilizing coding pattern in a in L_r-L_i channel on the *x*-*y* plane cutting at *z*=100 mm. (**d**) Numerically simulated and experimentally measured normalized electric field intensity of RCP component utilizing coding pattern in b in R_r-R_i channel on the *x*-*y* plane cutting at *z*=100 mm. (**e**) The target monochrome image of the letter "L" and corresponding phase coding patterns under the normal incidence of LCP waves. (**f**) The target monochrome image of the letter "R" and corresponding phase coding patterns under the normal incidence of RCP waves. (**g**) Numerically simulated and experimentally measured normalized electric field intensity of LCP component utilizing coding pattern in e in L_r-L_i channel on the *x*-*y* plane cutting at *z*=100 mm. h Numerically simulated and experimentally measured normalized electric field intensity of RCP component utilizing coding pattern in f in R_r-R_i channel on the *x*-*y* plane cutting at *z*=150 mm. All of the results are simulated and measured at frequency of 10 GHz.

Meanwhile, we have also evaluated the imaging quality via quantitative methods including the imaging efficiency defined as the ratio between the energy of the reconstructed image and the incident energy and the signal to noise ratio (SNR) defined as the ratio of the peak intensity in the imaging area to the standard deviation of the background noise. The measured imaging efficiencies and the SNRs of the generated letters are separately

14.32%, 16.11%, and 16.44 dB, 15.63 dB. Noticeably, we have also evaluated the performance of the meta-holograms with identical focal length at other frequencies provided in Section S8 (Supplementary information) and found that the simulated and measured normalized electric field intensities undergo negligible changes and are in good agreement with the target images in the matched channels in the frequency range of 9–10.5 GHz.

In the second demonstration, we use the proposed metasurface to generate meta-holograms with variable focal length. Likewise, two different target holographic images: letters "L" and "R" are prestored in L_r-L_i channel and R_r-R_i channel, respectively, as shown in the left panel of Fig. 3(e) and 3(f). It's worth noting that the reference frequencies are also selected at 10 GHz, but the holographic imaging planes for L_r-L_i channel and R_r-R_i channel are designed at z=100 mm and z=150 mm apart from the metasurface. The desired phase coding patterns for reconstructing the target images are separately calculated and presented in the right panel of Fig. 3(e) and 3(f). When LCP wave normally illuminates to the metasurface, holographic image of letter "L" will be generated in the reflection space; while RCP wave normally illuminates to the metasurface, holographic image of letter "R" will be generated in the reflection space, as depicted in Fig. 3(g) and 3(h). In addition, the measured imaging efficiencies and the SNRs of the generated letters are separately 15.36%, 20.32%, and 22.18 dB, 16.38 dB. In addition, the broadband performance of the meta-holograms with variable focal length is also achieved, and the simulated and measured results are provided in Section S9 (Supplementary information).

Versatile customization of meta-holograms with switchable spatial pixels

Manipulating continuous near-field distribution has been widely used in the applications of communication, encryption, anti-counterfeiting, and etc. Thereupon, in the third demonstration, we use the proposed metasurface to customize meta-holograms with switchable spatial pixels. Generally, the PO meta-hologram is equivalent to the superposition of multiple focal pixels and accomplished via compensating the phase between the focal pixel and the meta-particle. Through modifying different phase coding patterns applied to the metasurface, the discretized spatial pixels of the predesigned holographic image are supposed to move along the certain routes in x-y plane and ultimately form the trajectory of the target image. Subsequently, take the holographic image of letter "S" as an example for illustration, and the scanning trajectory is split into upper-half and lower-half regions in both channels where the counterclockwise yellow and green arrows respectively represent L_r-L_i and R_r-R_i channels, as shown in Fig. 4(a). Accordingly, as displayed in Fig. 4(b), four groups of sequentially and synchronously switched spatial pixels ($\sigma_{-,1}$, $\sigma_{+,1}$), ($\sigma_{-,2}$, $\sigma_{+,2}$), ($\sigma_{-,3}$, $\sigma_{+,3}$), ($\sigma_{-,4}$, $\sigma_{+,4}$) are selected to generate the holographic image.

Under the illumination of LCP wave, each of the four spatial pixels including $\sigma_{-,1}$, $\sigma_{-,2}$, $\sigma_{-,3}$, $\sigma_{-,4}$ exhibited in the left panel of Fig. 4(b) are individually designed and sequentially implemented. Herein, the reference frequency and imaging plane are designated at 10 GHz and at z=100 mm apart from the metasurface. Combined with the iterative optimization algorithm, four discretized phase coding patterns are achieved for generating the corresponding spatial pixels in L_r-L_i channel, as shown in Fig. 4(c–f). The simulated and measured results at the observational plane of z=100 mm are shown in Fig. 4(g-j), where the spatial pixels can be scanned along the trajectory of lower-half letter "S". Moreover, the simulated and measured broadband performance of the meta-holograms with switchable spatial pixels for LCP incidence is provided in Section S10 (Supplementary information).

In accordance with the operation method of LCP incidence, when RCP wave illuminates the CBR-CM, each of the four spatial pixels including $\sigma_{+,1}$, $\sigma_{+,2}$, $\sigma_{+,3}$, $\sigma_{+,4}$ exbitited in the right panel of Fig. 4(b) is also individually designed and sequentially implemented. At the condition that reference frequency of 10 GHz and focusing plane of z=100 mm, Fig. 4(k–n) depict four discretized phase coding patterns designed for generating the corresponding spatial pixels in R_r-R_i channel. It can be observed from the simulated and measured results at the observational plane of z=100 mm of Fig. 4(o–r) that the spatial pixels can also be scanned along the trajectory of upper-half letter "S". In addition, the simulated and measured broadband performance of the meta-holograms with switchable spatial pixels for RCP incidence is provided in Section S10 (Supplementary information). Since the complete holographic image of letter "S" comprises eight different spatial pixels, therefore, the measured imaging efficiency and SNR are specifically equivalent to the efficiency summation and the mean SNR value of eight focal pixels and separately calculated as 12.62% and 18.43 dB. Note that here we only take eight specific cases

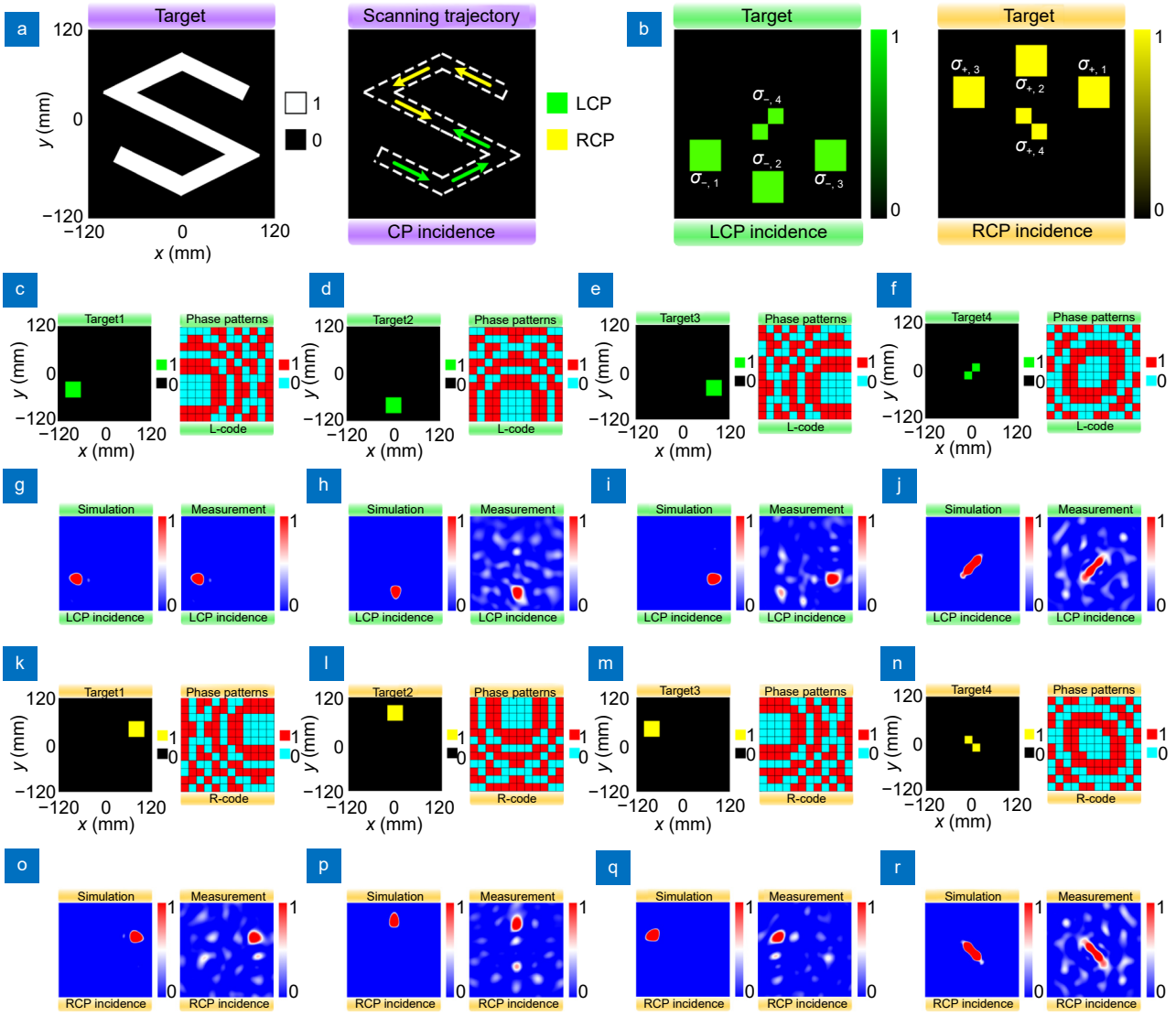

Fig. 4 | Multifunctional customization of meta-holograms with switchable spatial pixels. (**a**) The target monochrome image of the letter "S" and scanning trajectory of LCP and RCP spatial pixels under the normal incidence of orthogonal CP waves. (**b**) Four groups of sequentially and synchronously switched spatial pixels ($\sigma_{-,1}$, $\sigma_{+,1}$), ($\sigma_{-,2}$, $\sigma_{+,2}$), ($\sigma_{-,3}$, $\sigma_{+,3}$) and ($\sigma_{-,4}$, $\sigma_{+,4}$) distributions in L_r-L_i and R_r-R_i channels, respectively. The subscript "-" and "+" represent the LCP and RCP reflection channels. (**c**–**f**) The target monochrome image and phase coding patterns of spatial pixel $\sigma_{-,1}$, $\sigma_{-,2}$, $\sigma_{-,3}$, and $\sigma_{-,4}$. (**g**–**j**) The corresponding simulated and measured normalized electric field intensity of LCP component on the *x*-*y* plane cutting at *z*=100 mm. (**k**–**n**) The target monochrome image and phase coding patterns of spatial pixel $\sigma_{+,1}$, $\sigma_{+,2}$, $\sigma_{+,3}$, and $\sigma_{+,4}$. (**o**–**r**) The corresponding simulated and measured normalized electric field intensity of RCP component on the *x*–*y* plane cutting at *z*=100 mm. All of the results are simulated and measured at frequency of 10 GHz.

of the allocated holographic image for examples to demonstrate the tunability of the scanning trajectory, and in fact, arbitrary-shaped pixel trajectory of arbitrary holographic image can be achieved via carefully designing the phase coding patterns. With the assistance of computer software, the theoretical results of these above-mentioned three groups of different holograms are calculated and provided in Section S11 (Supplementary information).

Cyclic evolution of meta-holograms against arbitrary polarization states on Poincaré sphere

In the above designed CBR-CM, only the capability in controlling the reflected waves of meta-holograms under orthogonal CP incidence is validated effectively. Here, considering the good orthogonal polarization isolation of the proposed meta-particle, we further use the proposed metasurface to design the full-polarized detection system against the cyclic evolution of arbitrary polarization states on Poincaré sphere. It should be noted that though

all the polarizations of the EM wave can be represented by the Poincaré sphere, arbitrary polarization of the EM wave is a linear combination of orthogonal polarization basis vectors. Hence, any arbitrary polarization state $|n\rangle$ can be considered as the superposition of the orthogonal polarization state (in this paper, i.e., LCP and RCP states) with different amplitude and phase, as described as

$$|n\rangle = A_{\mathrm{L}}\mathrm{e}^{\mathrm{i}\delta_{\mathrm{L}}}|\boldsymbol{L}\rangle + A_{\mathrm{R}}\mathrm{e}^{\mathrm{i}\delta_{\mathrm{R}}}|\boldsymbol{R}\rangle \ , \tag{2}$$

where, $|\boldsymbol{L}\rangle$ and $|\boldsymbol{R}\rangle$ represent LCP and RCP states, respectively, A_{L}, A_{R} and δ_{L}, δ_{R} are the amplitude and phase coefficients of two CP waves. Consequently, the azimuth angle ψ and ellipticity angle χ of polarization ellipse corresponding to the $|n\rangle$ state can be derived based on vector decomposition and Stokes-Cartesian coordinate transformation as

$$\psi = \frac{\delta_{\mathrm{R}} - \delta_{\mathrm{L}}}{2},\ \chi = \frac{1}{2}\arcsin\left(\frac{A_{\mathrm{R}}^2 - A_{\mathrm{L}}^2}{A_{\mathrm{R}}^2 + A_{\mathrm{L}}^2}\right) \ . \tag{3}$$

In this way, an arbitrary full-polarization DOF, including orientation, ellipticity, and chirality of the reconstructed field, are determined via deducting the amplitude ratio $A_{\mathrm{R}}/A_{\mathrm{L}}$ and phase retardation δ_{R}-δ_{L}. Without loss of generality, we have chosen eight characteristic (states of polarization) SOPs as the incident wave to reconstruct the same holographic image of symbol "+", as shown in the left panel of Fig. 5(a). Likewise, the reference frequency and imaging plane are designated at 10 GHz and at z=100 mm apart from the metasurface. Attributed to the identical polarization state between the incident wave and reflected wave in the process of polarization detection, the phase coding patterns in the LCP and RCP reflection channels of the CBR-CM should also be maintained consistent, as displayed in middle and right panels of Fig. 5(a). From the point Ⅰ representing LP-0° state to point Ⅷ representing ERCP state, continuous evolution is experienced through LP-90° state (point Ⅱ), LP-45° state (point Ⅲ), LP-135° state (point Ⅳ), LCP state (point Ⅴ), RCP state (point Ⅵ), and ELCP state (point Ⅶ), where combined with vectorial decomposition of amplitude and phase relationship of orthogonal CP basis vectors, the self-defined characteristic parameters (ψ, χ) representing the azimuth angle and ellipticity angle of each polarization with their corresponding normalized amplitudes (r_{RR}, r_{LL}) and phase retardation $\Delta\varphi$ of these eight polarized incidence from Ⅰ to Ⅷ are detailedly listed in Table 1.

The numerically simulated and experimentally measured normalized electric field amplitudes and phase of LCP and RCP components are exhibited in Fig. 5(c–j). When the input polarization states are LP-0°, LP-90°, LP-45°, and LP-135° states, the output electric field distributions observed at the imaging plane all contain co-polarized components R_r-R_i and L_r-L_i, as shown in Fig. 5(c–f). It can be observed that the output polarized fields of the holographic images possess the same amplitudes but specific phase retardation of LCP and RCP components, where specifically, the amplitude intensities are basically around 0.707, and the phase retardation is 0°, 180°, 90°, and 270° in turn, which conforms well to the theoretical analysis in Table 1. It's worth emphasizing that attributed to 1-bit phase modulation of orthogonal CP incidence, the holographic images can also be generated under LP conversion channels, and the simulated results are provided in Section S12 (Supplementary information).

With the polarization states of incidence changing to LCP and RCP states, the output polarized fields of the holographic images denoted in Fig. 5(g) and 5(h) only include corresponding polarization basis vectors, and the phase distributions of LCP and RCP components exhibit no apparent relationship. Eventually, as illustrated in Fig. 5(i) and 5(j), under the illumination of ELCP and ERCP waves, the amplitude proportion of LCP and RCP components in the output polarized fields of the holographic images are approximately 1 : 0.27 and 0.27 : 1, and the phase differences are respectively around 120° and 300°, coinciding well with the decomposed orthogonal CP parameters presented in Table 1. According to the above evolution process, it can be confirmed that all polarization states on Poincaré sphere can be fully covered and detected, the amplitude and phase profiles between LCP and RCP components can be considered as function of the incident polarization. What's more, due to the non-dispersive performance of the phase modulation, the broadband performance of the meta-holograms under the excitation of eight polarizations are demonstrated via simulation and measurement and provided in Section S13 (Supplementary information). To further intuitively characterize the properties of the proposed CBR-CM, some relevant works are referred and the concrete performance comparisons are listed in Section S14 (Supplementary information).

Conclusions

To sum up, we have proposed and experimentally

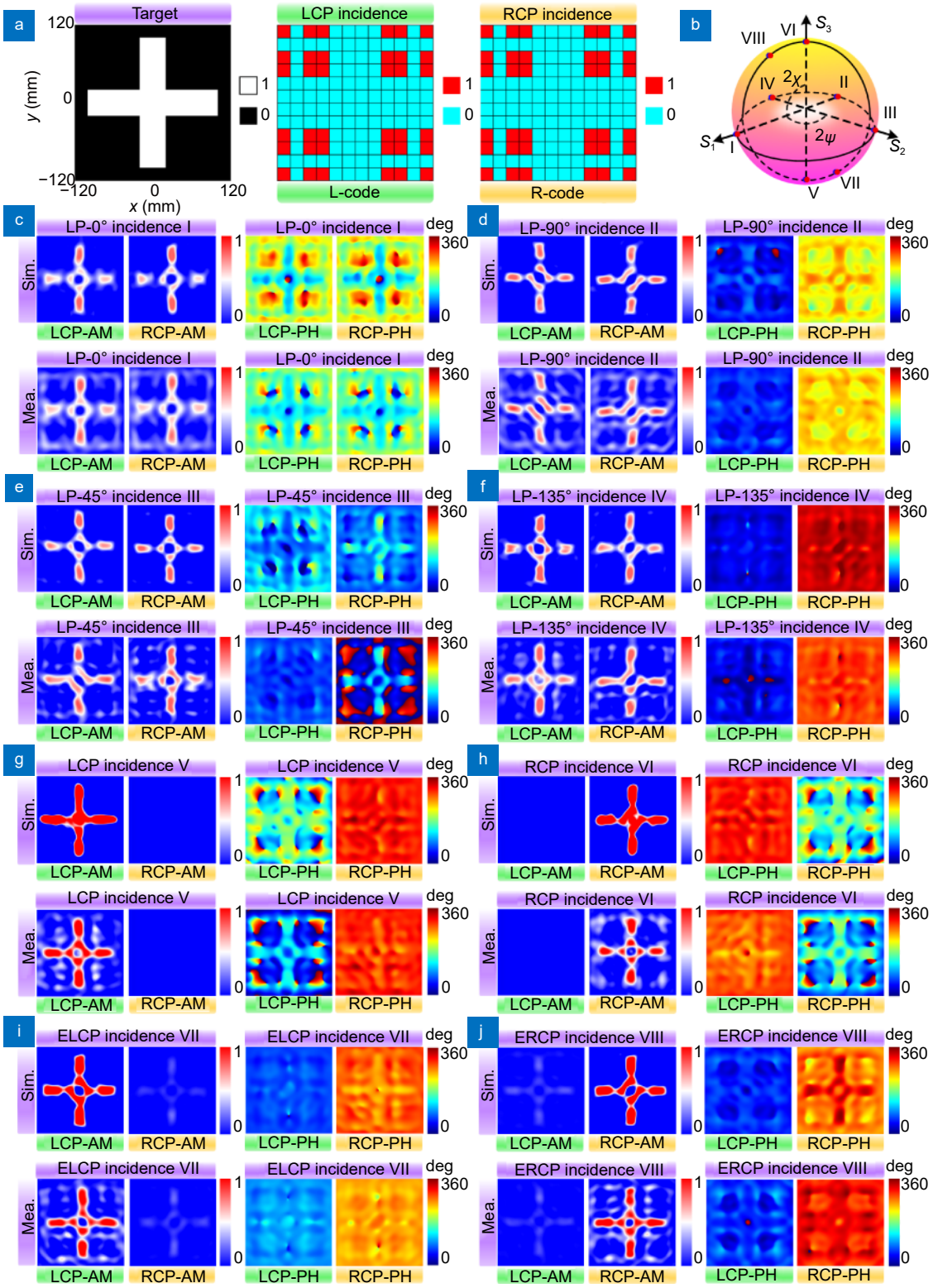

Fig. 5 | Cyclic evolution of meta-holograms against arbitrary polarization states on Poincaré sphere. (**a**) The target monochrome image of the symbol "+" and corresponding phase coding patterns of LCP basis vector and RCP basis vector. (**b**) schematic of eight typical SOPs on Poincaré sphere. The numerically simulated and experimentally measured amplitude and phase profiles of normalized electric field of LCP and RCP components under the normal incidence of (**c**) LP-0° (linear polarized vibrating along 0° angle with respect to horizontal axis), (**d**) LP-90°, (**e**) LP-45°, (**f**) LP-135°, (**g**) LCP, (**h**) RCP waves, (**i**) ELCP (elliptical left-handed circularly polarized), and (**j**) ERCP (elliptical right-handed circularly polarized) waves. All of the results are simulated and measured at frequency of 10 GHz.

Table 1 | Eight characteristic polarization states with their corresponding orthogonal CP states decomposition.

Polarization states	Characteristic parameters		Orthogonal decomposition		
	ψ	χ	r_{RR}	r_{LL}	$\Delta\varphi(\varphi_{RR}$-$\varphi_{LL})$
LP-0°	0°	0°	0.707	0.707	0°
LP-90°	45°	0°	0.707	0.707	180°
LP-45°	90°	0°	0.707	0.707	90°
LP-135°	135°	0°	0.707	0.707	270°
LCP	-	−45°	0	1	-
RCP	-	45°	1	0	-
ELCP	60°	−30°	0.2588	0.9659	120°
ERCP	150°	30°	0.9659	0.2588	300°

demonstrated a complete-basis-reprogrammable coding metasurface paradigm which empowers on-demand, direct, real-time holographic patterns dynamic reconstruction under arbitrary polarization states. The proposed CBR-CM is composed of an array of dynamically reconfigurable meta-particles ingeniously embedded with two symmetrical PIN diodes, which can modulate the co-polarized reflection phase responses with high-uniform amplitudes via tailoring FPGA-controlled bias voltages of the diodes and simultaneously introducing dynamic AA phase induced through the path effect in co-polarized reflection channels. Various and sophisticated holographic functions have been achieved via optimizing 1-bit phase coding patterns based on the iterative optimization algorithm. As proofs of concept, we designed, fabricated, and characterized a CBR-CM prototype, from which four completely different holographic meta-devices, including spin-controlled meta-holograms with identical and variable focal length, coplanar dual-polarized pixel synthesis exhibiting the independently customizable holograms within orthogonal CP channels, and full-polarized detection system on Poincaré sphere with the assistance of vectorial decomposition and synthesis showcasing the controllability of holograms under arbitrary polarization states. The measured results are in coincidence with the numerical simulations and with good performance. Generating more meta-holograms with arbitrary output polarization states in consistent with the incident excitation can be engineered via combination of rheostatic and varactor diodes, which is further extension of current approach. Overall, our CBR-CM proposal provides a powerful and flexible working platform for more advanced and multifunctional equipment with multiple independent information channels, potentially contributing to the development of future-oriented high-integrated and multi-task intelligent wireless imaging systems, including data encryption, AR/VR displays, and 3D projection.

Materials and methods

Simulation Setup

In this work, all simulations were performed via using CST Microwave Studio. The simulations of the meta-particle were carried out by finite-difference frequency-domain (FDFD) technique, in which the boundary conditions of the "unit cell" were set along *x*- and *y*-directions, and two Floquet ports were fixed at ±*z* directions. The full-wave simulations of the CBR-CM were implemented via finite-difference time-domain (FDTD) technique. The boundary conditions of "open (add space)" were set along *x*-, *y*-, and *z*-directions, and a plane wave source encoded with predesigned polarizations was fixed at +*z* direction for normal incidence.

FPGA-based Control circuit

A FPGA-based control circuit was designed and introduced to address each super-cell, as depicted in Section S15 (Supplementary Information). A FPGA (Alinx Altera cyclone Ⅵ) was selected as the main controller of the control circuit. The FPGA was connected to the server based on Transmission Control Protocol/Internet Protocol stack, and then command messages containing the information of the 1-bit phase coding patterns were received and processed to configure bias voltages applied on CBR-CM. The FPGA-based control circuit provides 288 independent voltage channels, and every two channels were connected to the same supercell to achieve joint control of the left and right PIN diodes. A high precision regulated power supplier was used to provide bias voltages to control CBR-CM and power all chips in the circuit. High precision analog multiplexers were used to reduce the complexity and cost of the control circuit, and

input/output (I/O) expanders were chosen to extend I/O pins of the FPGA through inter-integrated circuit protocol.

Prototype fabrication

The CBR-CM prototype was fabricated by industry-standard printed circuit board (PCB) technic. Then 1152 PIN diodes were embedded at the gaps of the meta-particles through machine welding procedure, which includes three crucial procedures that needs to be fulfilled: 1. Tin solder was added to the reserved solder pads; 2. PIN diodes were put onto the reserved pad position; 3. the tin solder melted and the diode and solder pads on the board were connected together through reflow soldering. The fabricated sample was with an overall dimension of 260 mm along x-axis and 250 mm along y-axis. The 0.25 mm-thickness DC bias layer and the 4 mm-thickness functional layer were connected by a 0.18 mm-thickness adhesive layer. Meanwhile, it should be noted that the alignment between different structural layers is achieved by external positioning holes calibrated by laser and riveted edges. The total profile of the DRSMC metasurface prototype was 4.43 mm ($0.148\lambda_0$ at 10 GHz). More details of the fabricated prototype are provided in Section S16 (Supplementary information).

Experimental setup

The near-field experiments in this paper were carried out in a standard microwave anechoic chamber to reduce the unnecessary EM interference in ambience, and more details of the experimental setups are provided in Section S16 (Supplementary information). In the near-filed measurements, the LP or CP horn antenna as the transmitter was placed $25\lambda_0$ apart from the CBR-CM prototype which was vertically set on the supporting foam on the experimental platform, and the scanning coaxial probe as the receiver was placed in front of the CBR-CM prototype with distance of focal length z. In addition, the transmitter antenna and the probe were connected to two ports of an Agilent N5224A vector network analyzer, respectively. More specifically, the probe located in the center of the imaging plane was driven by the motion controller with the fixed step of 5 mm along both x- and y-directions to measure the amplitude and phase profiles of the electric field in 240×240 mm^2 region, and the measurement system can record the electric field data synchronously. Since the electric field for the incidence of CP waves cannot be directly obtained, then according to the formulas $E_{\mathrm{LCP}}=\frac{\sqrt{2}}{2}(E_x+\mathrm{i}E_y)$ and $E_{\mathrm{RCP}}=\frac{\sqrt{2}}{2}(E_x-\mathrm{i}E_y)$ where E_x and E_y represent x- and y-LP fields. Accordingly, the electric field in other polarization channels can be further characterized via the decomposition relationship of CP basis vectors corresponding to characteristic polarization states provided in Table 1.

References

1. Yu NF, Genevet P, Kats MA et al. Light propagation with phase discontinuities: generalized laws of reflection and refraction. *Science* **334**, 333–337 (2011).
2. Huang L, Chang CC, Zeng BB et al. Bilayer metasurfaces for dual- and broadband optical antireflection. *ACS Photonics* **4**, 2111–2116 (2017).
3. Rubin NA, Shi ZJ, Capasso F. Polarization in diffractive optics and metasurfaces. *Adv Opt Photonics* **13**, 836–970 (2021).
4. Li LL, Zhao HT, Liu C et al. Intelligent metasurfaces: control, communication and computing. *eLight* **2**, 7 (2022).
5. Liu JY, Fan F, Tan ZY et al. Terahertz cascaded metasurfaces for both spin-symmetric and asymmetric beam diffractions with active power distribution. *APL Photonics* **8**, 096112 (2023).
6. Fan JX, Li ZL, Xue ZQ et al. Hybrid bound states in the continuum in terahertz metasurfaces. *Opto-Electron Sci* **2**, 230006 (2023).
7. Zhu RC, Wang JF, Sui S et al. Chameleon-like intelligent camouflage metasurface. *Mater Des* **235**, 112422 (2023).
8. Li SJ, Li ZY, Liu XB et al. Transmissive digital coding metasurfaces for polarization-dependent dual-mode quad orbital angular momentum beams. *ACS Appl Mater Interfaces* **15**, 23690–23700 (2023).
9. Li J, Zheng CL, Li JT et al. Terahertz wavefront shaping with multi-channel polarization conversion based on all-dielectric metasurface. *Photonics Res* **9**, 1939–1947 (2021).
10. Shen ZY, Zhang QH, Huang XJ et al. Simultaneous transmissive and reflective polarization conversion cross different operating bands in a single metasurface. *Opt Laser Technol* **169**, 110071 (2024).
11. Wu GB, Zhu SY, Pang SW et al. Superheterodyne-inspired waveguide-integrated metasurfaces for flexible free-space light manipulation. *Nanophotonics* **11**, 4499–4514 (2022).
12. Zhao F, Li ZP, Li S et al. Terahertz metalens of hyper-dispersion. *Photonics Res* **10**, 886–895 (2022).
13. Li JX, Yuan YY, Yang GH et al. Hybrid dispersion engineering based on chiral metamirror. *Laser Photonics Rev* **17**, 2200777 (2023).
14. Zhu RC, Wang JF, Qiu TS et al. Direct field-to-pattern monolithic design of holographic metasurface via residual encoder-decoder convolutional neural network. *Opto-Electron Adv* **6**, 220148 (2023).
15. Zhang XY, Cheng JQ, Yue WJ et al. Twofold optical display and encryption of binary and grayscale images with a wavelength-multiplexed metasurface. *Nanophotonics* **12**, 3747–3756 (2023).
16. Ma Q, Gao W, Xiao Q et al. Directly wireless communication of human minds via non-invasive brain-computer-metasurface platform. *eLight* **2**, 11 (2022).

17. Hou TY, Li XT, Luo H et al. Optically-transparent meta-window for wireless communication. *Opt Express* **31**, 38949–38957 (2023).
18. Pan YB, Lan F, Zhang YX et al. Dual-band multifunctional coding metasurface with a mingled anisotropic aperture for polarized manipulation in full space. *Photonics Res* **10**, 416–425 (2022).
19. Han ZX, Wang F, Sun JH et al. Recent advances in ultrathin chiral metasurfaces by twisted stacking. *Adv Mater* **35**, 2206141 (2023).
20. Yuan YY, Wu Q, Burokur SN et al. Chirality-assisted phase metasurface for circular polarization preservation and independent hologram imaging in microwave region. *IEEE Trans Microwave Theory Tech* **71**, 3259–3272 (2023).
21. Shang GY, Li HY, Wang ZC et al. Transmission-reflection-integrated multiplexed janus metasurface. *ACS Appl Electron Mater* **3**, 2638–2645 (2021).
22. Mu YH, Qi JR, Xia SY et al. Non-interleaved bilayer complex-amplitude janus metasurface enabling energy-tailorable bidirectional wave modulation. *Laser Photonics Rev* **17**, 2200659 (2023).
23. Chen SQ, Xie ZQ, Ye HP et al. Cylindrical vector beam multiplexer/demultiplexer using off-axis polarization control. *Light Sci Appl* **10**, 222 (2021).
24. Zhang F, Guo YH, Pu MB et al. Meta-optics empowered vector visual cryptography for high security and rapid decryption. *Nat Commun* **14**, 1946 (2023).
25. Balthasar Mueller JP, Rubin NA, Devlin RC et al. Metasurface polarization optics: independent phase control of arbitrary orthogonal states of polarization. *Phys Rev Lett* **118**, 113901 (2017).
26. Cui TJ, Qi MQ, Wan X et al. Coding metamaterials, digital metamaterials and programmable metamaterials. *Light Sci Appl* **3**, e218 (2014).
27. Liu S, Cui TJ, Zhang L et al. Convolution operations on coding metasurface to reach flexible and continuous controls of terahertz beams. *Adv Sci* **3**, 1600156 (2016).
28. Cui TJ, Liu S, Li LL. Information entropy of coding metasurface. *Light Sci Appl* **5**, e16172 (2016).
29. Wu RY, Shi CB, Liu S et al. Addition theorem for digital coding metamaterials. *Adv Opt Mater* **6**, 1701236 (2018).
30. Zhang C, Cao WK, Yang J et al. Multiphysical digital coding metamaterials for independent control of broadband electromagnetic and acoustic waves with a large variety of functions. *ACS Appl Mater Interfaces* **11**, 17050–17055 (2019).
31. Jiao P, Mueller J, Raney JR et al. Mechanical metamaterials and beyond. *Nat Commun* **14**, 6004 (2023).
32. Wang YH, Sha W, Xiao M et al. Deep-learning-enabled intelligent design of thermal metamaterials. *Adv Mater* **35**, 2302387 (2023).
33. Li JT, Wang GC, Yue Z et al. Dynamic phase assembled terahertz metalens for reversible conversion between linear polarization and arbitrary circular polarization. *Opto-Electron Adv* **5**, 210062 (2022).
34. Wang ZD, Qian C, Lin PJ et al. 3D Intelligent Cloaked Vehicle Equipped with Thousand-Level Reconfigurable Full-Polarization Metasurfaces. *Adv Mater*, 2400797 (2024).
35. Wan X, Xiao CK, Huang H et al. Joint modulations of electromagnetic waves and digital signals on a single metasurface platform to reach programmable wireless communications. *Engineering* **8**, 86–95 (2022).
36. Li RJ, Liu HX, Xu P et al. Light-controlled metasurface with a controllable range of reflection phase modulation. *J Phys D Appl Phys* **55**, 225302 (2022).
37. Xu Q, Su XQ, Zhang XQ et al. Mechanically reprogrammable pancharatnam-berry metasurface for microwaves. *Adv Photonics* **4**, 016002 (2022).
38. Zhang L, Cui TJ. Space-time-coding digital metasurfaces: principles and applications. *Research* **2021**, 9802673 (2021).
39. Wang HL, Ma HF, Cui TJ. A polarization-modulated information metasurface for encryption wireless communications. *Adv Sci* **9**, 2204333 (2022).
40. Jiang LX, Li YF, Zheng L et al. Smart metasurface for active and passive cooperative manipulation of electromagnetic waves. *ACS Appl Mater Interfaces* **14**, 54359–54368 (2022).
41. Wang CH, Xu HX, Wang YZ et al. Reconfigurable transmissive metasurface synergizing dynamic and geometric phase for versatile polarization and wavefront manipulations. *Mater Des* **225**, 111445 (2023).
42. Liu TH, Meng YY, Wang JF et al. Six-channel programmable coding metasurface simultaneously for orthogonal circular and linear polarizations. *Photonics Res* **11**, 1047–1056 (2023).
43. Ma Q, Bai GD, Jing HB et al. Smart metasurface with self-adaptively reprogrammable functions. *Light Sci Appl* **8**, 98 (2019).
44. Krasikov S, Tranter A, Bogdanov A et al. Intelligent metaphotonics empowered by machine learning. *Opto-Electron Adv* **5**, 210147 (2022).
45. Zeng C, Lu H, Mao D et al. Graphene-empowered dynamic metasurfaces and metadevices. *Opto-Electron Adv* **5**, 200098 (2022).
46. Kim I, Jeong H, Kim J et al. Dual-band operating metaholograms with heterogeneous meta-atoms in the visible and near-infrared. *Adv Opt Mater* **9**, 2100609 (2021).
47. Park C, Kim W, Kim Y et al. High-throughput fabrication of large-scale metaholograms via one-step printing. *Adv Opt Mater* **12**, 2301562 (2024).
48. Kim J, Jeon D, Seong J et al. Photonic encryption platform *via* dual-band vectorial metaholograms in the ultraviolet and visible. *ACS Nano* **16**, 3546–3553 (2022).
49. Mehmood MQ, Seong J, Naveed MA et al. Single-cell-driven trichannel encryption meta-displays. *Adv Sci* **9**, 2203962 (2022).
50. Naveed MA, Ansari MA, Kim I et al. Optical spin-symmetry breaking for high-efficiency directional helicity-multiplexed metaholograms. *Microsyst Nanoeng* **7**, 5 (2021).
51. Li Y, Huang XJ, Liu SX et al. Metasurfaces for near-eye display applications. *Opto-Electron Sci* **2**, 230025 (2023).
52. Jung C, Kim G, Jeong M et al. Metasurface-driven optically variable devices. *Chem Rev* **121**, 13013–13050 (2021).
53. Kim J, Seong J, Yang Y et al. Tunable metasurfaces towards versatile metalenses and metaholograms: a review. *Adv Photonics* **4**, 024001 (2022).
54. So S, Kim J, Badloe T et al. Multicolor and 3D holography generated by inverse-designed single-cell metasurfaces. *Adv Mater* **35**, 2208520 (2023).
55. Li LL, Cui TJ, Ji W et al. Electromagnetic reprogrammable coding-metasurface holograms. *Nat Commun* **8**, 197 (2017).
56. Li LL, Ruan HX, Liu C et al. Machine-learning reprogrammable metasurface imager. *Nat Commun* **10**, 1082 (2019).
57. Wu LW, Ma HF, Wu RY et al. Transmission-reflection controls and polarization controls of electromagnetic holograms by a re-

configurable anisotropic digital coding metasurface. *Adv Opt Mater* **8**, 2001065 (2020).

58. Wang H, Qin Z, Huang LL et al. Metasurface with dynamic chiral meta-atoms for spin multiplexing hologram and low observable reflection. *PhotoniX* **3**, 10 (2022).

Acknowledgements

This work was supported by the National Natural Science Foundation of China (62101588), the National Key Research and Development Program of China (SQ2022YFB3806200), the Young Talent Fund of Association for Science and Technology in Shaanxi (20240129), and the Postdoctoral Fellowship Program of CPSF (GZC20242285).

Author contributions

Z. T. Chu and X. Q. Cai conceived the idea, theoretically designed and fabricated the samples, performed the FDFD and FDTD simulations, and conducted the experiments. R. C. Zhu, T. H. Liu, and H. T. Sun partially conducted the simulations and measurements. T. F. Li, Y. X. Jia, and Y. J. Han analyzed the results and made additional efforts in preparing the manuscript. Z. T. Chu and X. Q. Cai wrote the manuscript with input from all authors. S. B. Qu and J. F. Wang suggested the designs, and supervised the work. All authors discussed the results and commented on the manuscript.

Competing interests

The authors declare no competing financial interests.

Supplementary information

Supplementary information for this paper is available at https://doi.org/10.29026/oea.2024.240045